Stochastic Dynamics of Coastal Dune Vegetation

JGR Earth Surface

RESEARCH ARTICLE
10.1029/2025JF008610

Stochastic Dynamics of Coastal Dune Vegetation

C. Camporeale[1] and M. Latella[2]

[1]Department of Environment, Land and Infrastructure Engineering (DIATI), Politecnico di Torino, Torino, Italy, [2]CMCC Foundation—Euro-Mediterranean Center on Climate Change, Lecce, Italy

Abstract This work introduces a physically based modeling framework to capture the spatio-temporal dynamics of dune vegetation under stochastic environmental disturbances. The model evaluates vegetation cover in response to random wind speed and runup within a cross-shore dimensionless framework. The wind speed is modeled as a compound Poisson process with Gamma-distributed properties, facilitating the computation of up-crossing times for various thresholds. The dune topography is represented by a swash zone with a Gaussian shape and a monotonic landward increase, parameterized by slope, wavelength, and height. Key disturbance conditions affecting vegetation, that is, runup-induced flooding in the swash zone and wind-induced scour on the backshore and crest, are addressed through threshold-based analysis. The model uses a state-dependent dichotomic process for vegetation dynamics, where growth and decay are influenced by external forcing and vegetation state. Analytical solutions of the master equation for the vegetation distributions reveal the impact of stochastic factors on vegetation growth and stability. Sensitivity analysis identifies dune steepness, forcing magnitude and variability, and relative roughness as critical parameters. These factors significantly affect vegetation distribution, with increased steepness leading to higher vegetation density at the backshore and reduced density at the shorefront. Validation is carried out against satellite imagery and high-resolution real elevation data from the U.S. coastline and confirms the robustness and accuracy of the proposed approach. The results enhance understanding of dune vegetation dynamics and offer a framework for coastal restoration strategies.

Plain Language Summary Coastal sand dunes provide several ecosystem services, among which are recreational ones, flood protection, and carbon storage. However, they are endangered by rising sea levels, climate change, and urban development, which reduce their ability to provide the above mentioned services. In this work, we present a model to understand how coastal dune vegetation responds to changing environmental conditions like wind and wave runup. By focusing on one-dimensional dune profiles, the model makes it easier to study how different factors, for example, steepness and wind variability, impact vegetation growth and stability. The findings reveal how vegetation patterns shift with environmental changes, influencing dune stability and erosion. Validated using real-world satellite and open global data of hourly wind signals, this model provides valuable insights for coastal management and restoration efforts.

Special Collection:
Forcing, response, and impacts of coastal storms in a changing climate

Key Points:

- We present a model to capture dune vegetation dynamics under random wind and run-up disturbances, validated with Earth Observation data
- We reveal how factors like wind variability, dune steepness, and roughness impact vegetation patterning
- The findings offer insights into coastal dune management, helping design effective restoration strategies against environmental threats

Supporting Information:

Supporting Information may be found in the online version of this article.

Correspondence to:
C. Camporeale,
carlo.camporeale@polito.it

Citation:
Camporeale, C., & Latella, M. (2025). Stochastic dynamics of coastal dune vegetation. *Journal of Geophysical Research: Earth Surface*, *130*, e2025JF008610. https://doi.org/10.1029/2025JF008610

Received 26 MAY 2025
Accepted 12 OCT 2025

Author Contributions:
Conceptualization: C. Camporeale
Data curation: C. Camporeale
Formal analysis: C. Camporeale
Methodology: C. Camporeale
Software: C. Camporeale, M. Latella
Supervision: C. Camporeale
Validation: C. Camporeale, M. Latella
Visualization: M. Latella
Writing – original draft: C. Camporeale
Writing – review & editing: M. Latella

1. Introduction

Coastal sand dunes provide a multitude of essential ecosystem services, serving as recreational areas, critical habitats for threatened and endangered species, and protective buffers for human settlements against marine hazards (Davidson-Arnott, 2010; Martínez et al., 2008), in addition to representing significant reservoirs of *blue carbon* (Beaumont et al., 2014; Macreadie et al., 2019). However, despite over one-third of the global population residing within 100 km of the coastline (Reimann et al., 2023), coastal sand dunes face endangerment, losing their protective capacity, making some major cities increasingly vulnerable to marine floods (Hallegate et al., 2013). In various regions, dunes are threatened by a phenomenon known as *coastal squeeze*, which results from the combined effects of rising sea levels and intensified storminess due to climate change on one side, and urban and farmland sprawl on the other, causing the complete inhibition of their morphological and ecological dynamics (Doody, 2013).

Vegetated dunes are biogeomorphological systems that evolve through the continuous co-adjustment of abiotic and biotic elements (Figure 1a, see also Hesp (1991) and Maun (2009)). The primary physical disturbances of such systems are stochastic abiotic forces, including water level fluctuations (i.e., due to variations in sea level, tides, and waves), precipitation, and wind-mediated transport of sediments and salt along the coastline. The biotic component, comprising vegetation, biological soil crusts, and fauna, can modulate these forces, exerting

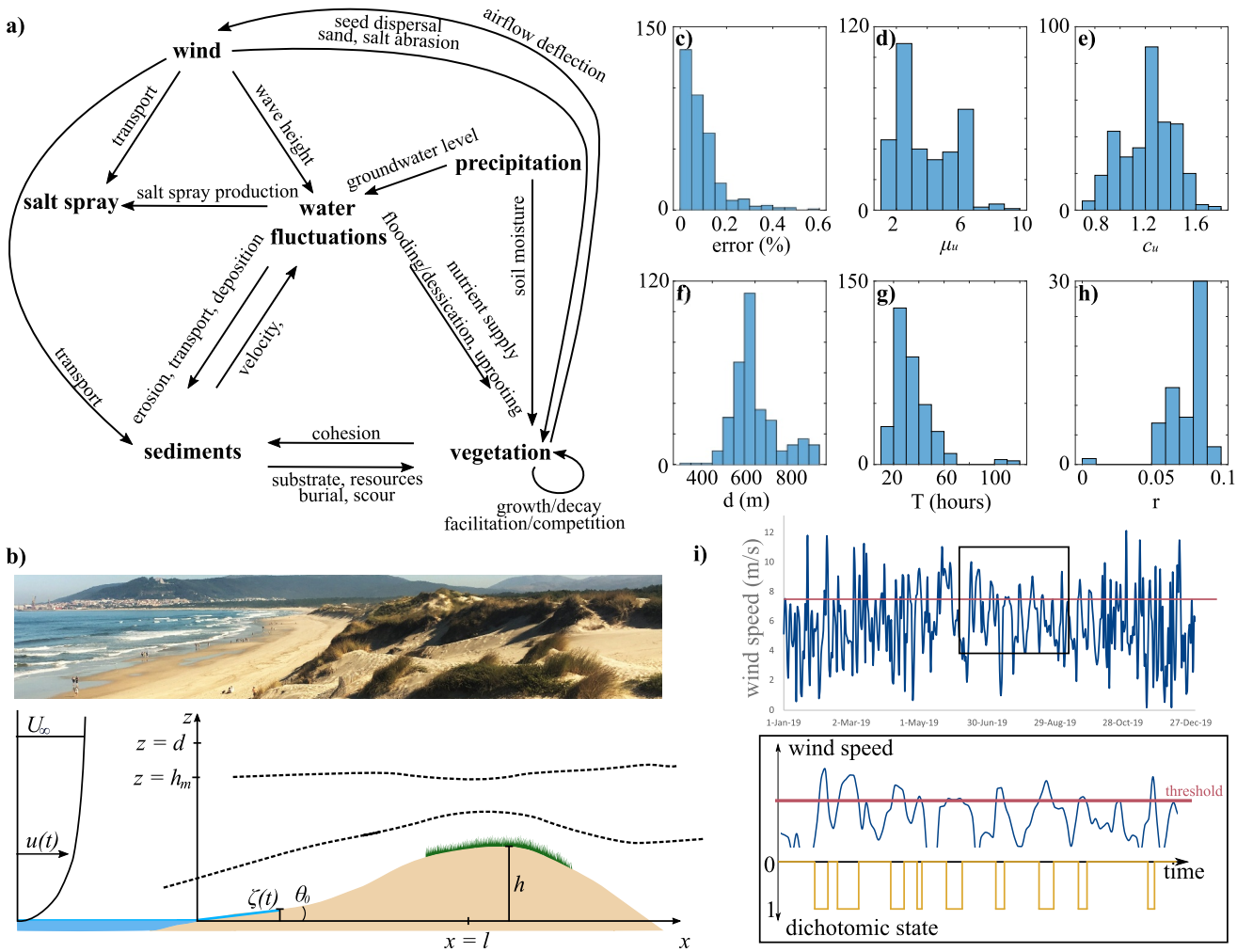

Figure 1. (a) Conceptual model of biogeomorphological feedback in coastal dune systems. (b) Geometrical setup of the model and comparison with a real coastal dune system and wind profile, where d is the height of the atmospheric boundary layer, and h_m is the height of the middle layer (sensu, Hunt et al., 1988). Dashed black lines qualitatively represent air flow over the dune profile. (c–h) Count distribution of hourly signals retrieved from the ERA5 data set (2019–2022). The analysis focuses on 336 cell points selected from 11 onshore zones adjacent to coastal areas characterized by minimally anthropized dunes (see Supporting Information S1 for details, Figure S1, Table S1). In details: (c) relative error computed as the L_2-norm of difference between the actual pdf of $u(t)$ and a Gamma distribution having the same mean and variance; (d) mean wind velocity; (e) coefficient of variation of wind velocity; (f) boundary layer height; (g) integral time scale of wind velocity, and (h) fitting coefficient of the relation $\zeta_{dw} = ru^2/g$. (i) Examples of mean daily wind speed from the ERA5 data set at Padre Island (26°48′36″N–97°24′14″W, CA, U.S.) and the relation between wind speed and the dichotomic status for a subset of the same time series.

additional influence on coastal landscape evolution (Bakker et al., 2023). In this work, we simplify the biotic component to vegetation only, but the proposed approach has the potential for extension to other ecosystem components.

The worldwide coastal vegetation exhibits similar adaptation strategies to cope with the numerous stressing factors that characterize these environments, such as sand burial and abrasion, swash inundation, ponding and erosion, wind exposure, salt spray, soil salinity, moisture and nutrient scarcity, lighting, and heat (Barbour et al., 1985; Hesp, 1991). Coastal vegetation is pivotal in initiating dune formation by promoting sand deposition (Bird, 2011; Maun, 2009). In turn, dune accretion provides new space for colonization, favoring the encroachment of dune-building species like *Ammophila Arenaria* (or beachgrass), while secondary species replace the former ones at a later stage (Belcore et al., 2024; Laing, 1958). Notably, plant dynamics promote dune stabilization since the mobility of sand decreases with increasing vegetation cover (i.e., the percentage of soil covered by plants), which shelters the soil and prevents wind entrainment.

Despite growing interest in research and policy concerning coastal areas and their adaptation to climate change (Toimil et al., 2020), only a limited number of biogeomorphological models for coastal dunes are available in the literature. Most of the existing models are numerical, owing to the inherent complexity of the feedback mechanisms they are intended to represent (Baas & Nield, 2007; Charbonneau et al., 2022; de Castro, 1995; de Luna et al., 2011; Durán Vinent & Moore, 2015; Keijsers et al., 2016; Moore et al., 2016; Nishimori & Tanaka, 2001; Van Dijk et al., 1999), although an analytical approach to foredune development was proposed by Durán Vinent and Moore (2013). These models primarily focus on the interactions between vegetation and sediment, with vegetation being characterized through variables such as percentage cover (Baas & Nield, 2007; Durán Vinent & Moore, 2013, 2015; Keijsers et al., 2016; Roelvink & Costas, 2019), average height (de Luna et al., 2011; Durán Vinent & Herrmann, 2006), density (de Castro, 1995; Nishimori & Tanaka, 2001; Roelvink & Costas, 2019), and, less frequently, biomass (Charbonneau et al., 2022). Among these descriptors, vegetation cover is the most commonly used due to its direct proportionality with the plant frontal area density, which influences the drag force exerted by wind (Durán Vinent et al., 2008).

Vegetation growth is often modeled using a logistic function (de Luna et al., 2011; Durán Vinent & Moore, 2013, 2015, 2019; Durán Vinent et al., 2008; Goldstein et al., 2017; Moore et al., 2016; Roelvink & Costas, 2019; Yizhaq et al., 2013), although alternative growth functions have been employed in some cases (Baas & Nield, 2007; Charbonneau et al., 2022; de Castro, 1995; Keijsers et al., 2016; Nishimori & Tanaka, 2001). Additionally, certain models incorporate the lateral spread of rhizomes and seed dispersal (Charbonneau et al., 2022; Goldstein et al., 2017; Keijsers et al., 2016; Moore et al., 2016; Yizhaq et al., 2013). Besides vegetation, all models consider sand height as a dynamic variable, except for Yizhaq et al. (2013), and none assume a static morphology. This is likely due to the relatively rapid growth of coastal dunes, which can increase in height by 0.01–0.1 m per year (Davidson-Arnott, 2010).

Three important aspects require further clarification in coastal dune morphodynamics and related models. First, the identification of key external disturbances has not been elucidated yet. Many approaches focus on wind-induced sand transport, while wind abrasion, precipitation, marine flooding, and groundwater have been rarely represented in models (Charbonneau et al., 2022; de Castro, 1995; de Luna et al., 2011; Durán Vinent & Moore, 2015; Keijsers et al., 2016; Yizhaq et al., 2013). Field observations show that both sand burial (Bel & Ashkenazy, 2014; Disraeli, 1984; Nolet et al., 2018; Wilson & Sykes, 1999) and salt spray (Barbour, 1978; Du & Hesp, 2020; Oosting, 1945) are primary disturbances to vegetation dynamics and the major drivers of coastal evolution, but models only account for the former. Second, models often disregard the role of stochastic noise characterizing environmental forcing, since most approaches are purely deterministic, apart from some reference to random erosion and transport probabilities (Keijsers et al., 2016), or to real noisy data in the simulations (Charbonneau et al., 2022; Durán Vinent & Moore, 2015). A notable exception, which provides the first stochastic model in this direction, has been proposed by Durán Vinent et al. (2021) and Ramakrishnan et al. (2024) for the barrier island elevation. However, no attempt has been made to model the role of stochastic wind in influencing vegetation patterns. Third, some modeling approaches establish a threshold value l_v, roughly corresponding to the distance between the dune crest and the shoreline and serving as a proxy for beach width. This definition aligns with the vegetation-free backshore width in other studies (de Luna et al., 2011), recognizing the crucial role of l_v in sediment supply and dune evolution.

To address the identified gaps in existing research, this study aims to achieve the following objectives: (a) develop a robust modeling approach to capture the dynamic interactions between vegetation distribution and abiotic factors in coastal sand dunes; (b) integrate descriptive ecological insights with a dichotomic stochastic approach by incorporating sediment transport; (c) investigate the influence of stochastic disturbances (noise) on coastal ecotones, providing analytical solutions for vegetation patterning; (d) offer a computational framework that leverages accessible input data from open global data sets, facilitating scalable and globally applicable modeling of coastal vegetation dynamics.

The overall purpose of this work is to unravel the impact of so-far underrated noise-induced wind forcing on coastal vegetated dune dynamics in terms of a threshold-guided state-dependent stochastic dichotomous equation. This approach allows vegetation dynamics to shift between two states—growth and decay—according to the random values assumed by wind-induced local disturbances. This probabilistic eco-hydrological model can determine vegetation patterning, providing a valuable tool to support further morphodynamic models for dune development. The present rationale partly recalls the framework of fluvial stochastic ecomorphodynamics

(Bertagni et al., 2018), justified by the shared similarities between coastal and riparian ecotones, despite the additional complexity introduced by salt spray and wind in the former. Indeed, in both cases, vegetation is subjected to stochastic forces, like water level fluctuations or sediment transport, which consist of both periodic and random components. These forces can have dichotomous effects—either supporting or disrupting vegetation—depending on whether certain tolerance thresholds are exceeded, thereby influencing the overall bio-geomorphological landscape evolution.

Although the model does not simulate the full morphodynamic evolution of dunes, its analytical framework provides a valuable tool for assessing how topographic and environmental parameters influence vegetation stability under stochastic forcing. By incorporating variables such as dune slope, roughness, and wind variability, the model enables scenario-based exploration of vegetation responses across a range of coastal settings. This makes it a potentially useful decision-support tool for restoration planning, allowing practitioners to evaluate the relative effects of different dune geometries or exposure regimes on vegetation persistence. In this way, the model offers a transferable process-based approach that can inform the design of dune restoration strategies, particularly when coupled with site-specific data from Earth observation or field monitoring.

In the following, the model construction is openly described (Sections 2 and 3). The sensitivity of the model to its main parameters is tested and discussed (Section 4), an overall validation is carried out leveraging freely available Earth Observation data (Section 5) and potential elements of the study transferable to real-world management actions are finally discussed (Section 6).

2. Materials and Methods

We defined a physically based minimal model, which, as also followed in Durán Vinent et al. (2021), reduces the complex two-dimensional dynamics of dune vegetation to a 1D spatio-temporal dynamics, just considering the variation in the cross-shore direction x (Figure 1b). The model addresses the response of a dimensionless vegetation cover index $\psi(x,t)$ to random disturbances represented by the wind speed $u(t)$, measured at the top h_m of the so-called middle layer of the atmospheric boundary layer, where the vertical velocity perturbation is maximum (see later), and the daily maximum runup $\zeta(t)$, computed with respect to the maximum tide (Figure 1b). The vegetation is assumed to establish on a quasi-steady mature dune morphology (*sensu* Ramakrishnan et al. (2024)). In the following, bracket notation will refer to the mean value of a random variable.

2.1. Statistical Characterization of the External Forcing

Wind speed is described here as a stochastic process with average $\mu_u = \langle u \rangle$, coefficient of variation c_u (i.e., standard deviation-to-mean ratio), integral timescale $\mathcal{I}_u$ (i.e., the integral of the autocorrelation function, namely the memory of the process), and a Gamma probability distribution function which is flexible enough for many practical cases (Ridolfi et al., 2011), namely,

$$p_u = \frac{c_u^{-2q}}{\mu_u \Gamma_q} \left(u/\mu_u\right)^{q-1} e^{-uq/\mu_u}, \tag{1}$$

where $q = c_u^{-2}$ and $\Gamma_q = \int_0^\infty t^{q-1} e^{-t} dt$ is a shorthand for the Euler Gamma function. Since $u(t)$ is an extremely intermittent variable, performing sudden shots with exponential decays on the daily timescale, it can be modeled robustly as a compound Poisson process, which is indeed Gamma-distributed, $\dot{u} = -u/\mathcal{I}_u + \zeta$, where $\zeta(t)$ is a shot noise with mean intervals between two pulses equal to $\mathcal{I}_u c_u^2$ and mean value $\mu_u c_u^2$, while dot refers to the time derivative. This kind of model is also called *marked Poisson process with exponentially distributed sizes* because the interarrival times of the shots and the mark of the jumps are both assumed exponentially distributed. We remark that this assumption is consistent with recent findings on the statistics of overtopping of a characteristic beach elevation (Kang et al., 2024; Rinaldo et al., 2021), which is a random process strictly related to wind forcing.

A further justification of the above choice based on statistical reanalysis of the ERA5 hourly wind data set (fifth generation of the European Centre for Medium-Range Weather Forecast) is illustrated in Figure 1c, where we analyzed hourly signal, from 2019 to 2023, of the following variables: (a) zonal and meridional components of the wind at a height of 100 m above the Earth's surface, $\mathbf{u}_{100}=(u_{100}, v_{100})$, (b) zonal and meridional components of the

wind at a height of 10 m above the Earth's surface, $\mathbf{u}_{10}=(u_{10}, v_{10})$; (c) boundary layer height, d; (d) significant height of wind waves, ζ_{dw}. These variables were downloaded through an API client (Application Programming Interface) from the Copernicus Climate Data Store (CDS), for a set of 336 grid points selected from 11 onshore zones adjacent to coastal areas of U.S., Mexico, France, Portugal and Australia, which are characterized by minimally anthropized dunes. A notable result is that the Gamma distribution fits the real data with errors typically less than 0.5%. More details on the ERA5 data set analysis are reported in Supporting Information S1, while the whole data set is deposited in Camporeale and Latella (2025).

The compound Poisson process allows for the use of a well-known exact result of stochastic theory (Laio et al., 2001), providing the up-crossing and down-crossing times, that is, the average time of u exceeding or not a certain threshold u^*, respectively, as

$$\langle t_{u>u^*}\rangle = \mathcal{I}_u e^{\hat{u}} E(1-q,\hat{u}), \qquad \langle t_{u<u^*}\rangle = \mathcal{I}_u\left(\frac{\Gamma_q}{\Gamma_{q,\hat{u}}}-1\right)e^{\hat{u}}E(1-q,\hat{u}), \tag{2}$$

where $\hat{u}=qu^*/\mu_u$, while $E(a,z)$ is the exponential integral function and $\Gamma_{a,b}=\int_b^\infty t^{a-1}e^{-t}dt$ is a shorthand for the incomplete Gamma function (Abramowitz & Stegun, 1964). Equation 2 are used in the following to compute the mean time the vegetation stays in comfort or stress conditions throughout the dune profile. In the event a real-time series were available for the wind variable, the above model might be easily replaced by the direct computation of the crossing times. A validation with real cases is reported in Section 5.

2.2. Topography and Hydrodynamics

The topography of mature dunes in coastal environments is the result of a complex time-dependent coevolution between sediment transport and vegetation (Zarnetske et al., 2012). For analytical purposes, the present theory adopts a simple, but versatile, dune shape that merges a linear *swash zone* near the shoreline with a Gaussian shape and a monotonic landward increase of elevation. This shape is described by three parameters: (a) the angle of slope of the swash zone, θ_0; (b) the wavelength of the dune, $2l$; (c) and its height, h. Notice that real topographies will be used in the validation section.

We consider z_0 as the wall roughness height (equal to 2.5 times the median sand diameter D_{50} for bare dunes, and increasing with vegetation density) so that a relative roughness $\xi=z_0/l$ can be introduced and, according to Hunt et al., 1988 we assume that the relevant upwind velocity u is measured at an intermediate height $h_m=(l/2)\log^{-1/2}(1/2\xi)$, see Figure 1, so $u:=U(h_m)$. After using l and $(gl)^{1/2}$ to non-dimensionalize lengths and velocities, respectively, three pure numbers emerge: the dune *steepness*, β, a (random) *windy Froude-like number*, F—again referring to the height of the middle layer of the boundary layer—and the *relative roughness*, ξ, respectively

$$\beta=\frac{h}{l}, \qquad F=\frac{u(t)}{\sqrt{gl}}, \qquad \xi=\frac{z_0}{l}. \tag{3}$$

In this dimensionless framework, the dune topography may, therefore, be represented as

$$\eta=\tan\theta_0 \arctan X+\beta e^{-4(X-1)^2}, \tag{4}$$

where $X=x/l$, so that $X=0$ marks the shoreline and $X=1$ corresponds to the position of the dune crest (Figure 2a).

Following well-established perturbation theories for a boundary layer interacting with an undulated topography (Fowler, 2011; Kroy et al., 2002), a dimensionless perturbative parameter ϵ is introduced as the ratio between friction velocity u_* and u. Assuming a log-law distribution for velocity, it is straightforward to show that ϵ and ξ are related through

$$\epsilon=\frac{u_*}{u}=-\frac{\kappa}{\log(2\xi\sqrt{-\log 2\,\xi})} \tag{5}$$

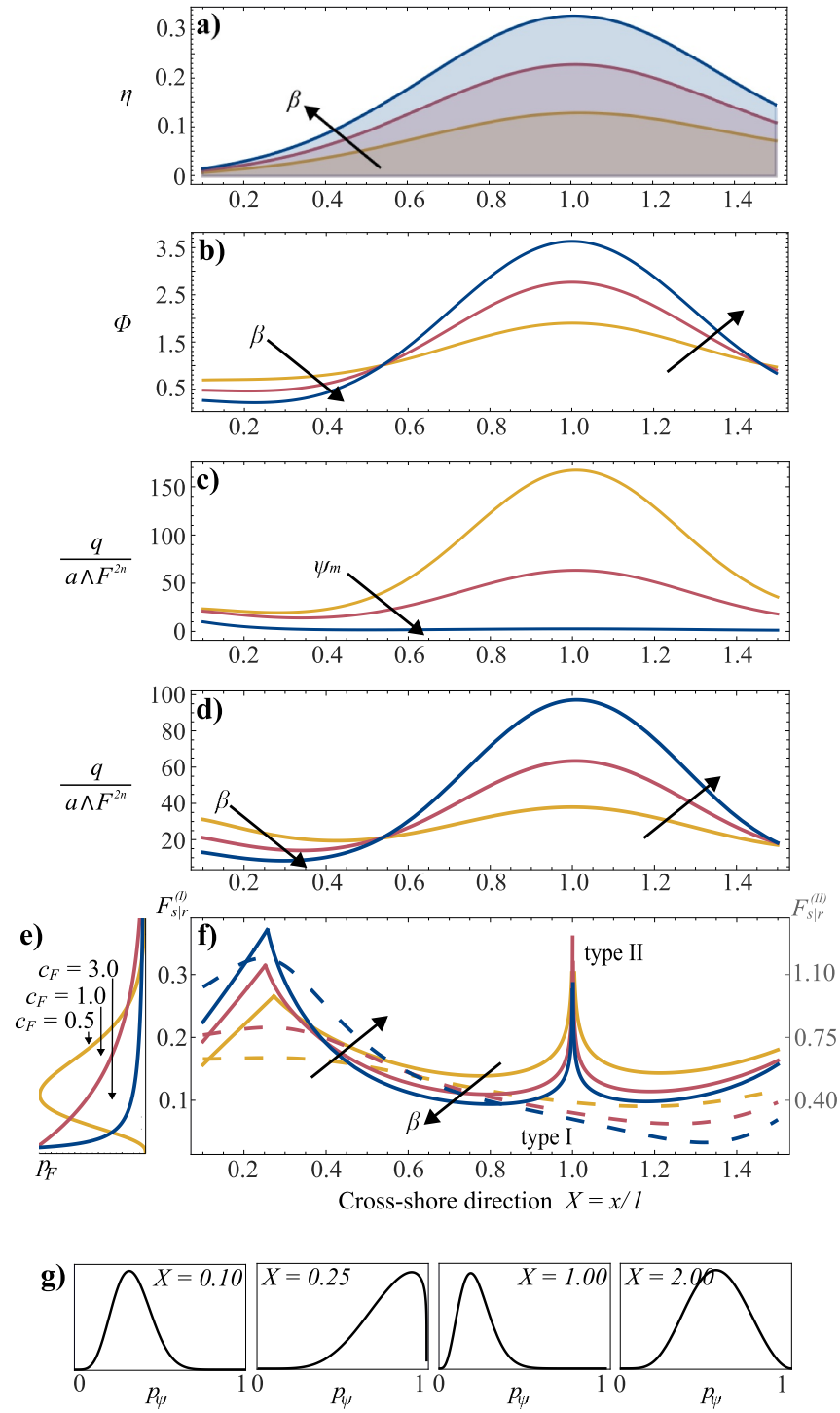

Figure 2. (a) Dune topography η. (b) The function Φ, characterizing the bed stress τ_* via Equations 8 and 9. (c) Distribution of the sediment transport q by assuming a vegetation profile identical to the dune shape and having a maximum value $\psi_m = [0.05,0.1,0.5]$ from yellow to blue but fixing β to 0.15. (d) Distribution of the sediment transport q by assuming a vegetation profile identical to the dune shape and having a maximum value fixed to $\psi_m = 0.1$, with $\beta = [0.1,0.15,0.2]$ from yellow to blue. (e) Examples of Gamma-distributed probability density function (pdf, p_F), $\mu_F = 0.1$ and varying c_F. (f) Values for the thresholds $F_{s|r} = \min(F_s,F_r)$ for type I (left) and type II (right). ($\theta_0 = 2°$; $\xi = 10^{-5}$; Yellow: $\beta = 0.1$; Red: $\beta = 0.2$; Blue: $\beta = 0.3$). (g) Example of pdfs of the vegetation cover p_ψ at different locations for vegetation type I, and $\{\beta, t_g/t_d, \mu_F, \mathcal{T}, c_F\} = \{0.15, 360/5, 0.05, 2/t_g, 2\}$.

with $\kappa = 0.41$ the von Karman. In the interval $\xi = 10^{-6} - 10^{-3}$ the above formula provides the values $\epsilon = 0.04 - 0.07$. The Jackson-Hunt theory accounts for the turbulent flow over a small hill (Hunt et al., 1988), and incorporates Prandtl's mixing layer theory through an asymptotic matching approach (a comprehensive and enhanced theory is presented in Chapter 5 of Fowler (2011)). Accordingly, the most crucial forcing of the present analysis, namely the bed shear stress, is expressed as

$$\frac{\tau}{\rho\epsilon^2 u^2} = 1 + f(\epsilon)\mathcal{H}(d\eta/dx) - \frac{4\epsilon}{\kappa}\int \frac{d\eta}{d\zeta}\frac{\log(x-\zeta)}{\pi(x-\zeta)}d\zeta + \frac{2\pi\epsilon}{\kappa}\frac{d\eta}{dx}, \tag{6}$$

where $f \sim 2 + 9.75\epsilon\log(3.56/\epsilon)$ and $\mathcal{H}(f) = \int \frac{f(\zeta)}{\pi(x-\zeta)}d\zeta$ is the so-called Hilbert transform. Typical values of ϵ reduce the last two terms negligible with respect to the first two.

3. Threshold-Induced Dichotomic Vegetation Model

To assess the temporal dynamics of vegetation, it is customary to refer to a dimensionless time, $T = t/t_g$, where t_g is a characteristic time for vegetation growth. In the present work, we assume that t_g is much shorter than the morphodynamic time scale $t_m \sim t_g/|\dot{\eta}|$ (where $\dot{\eta}$ refers to the time derivative of the topography in the dimensionless framework), according to the quasi-steady approximation. This assumption is reasonable for grasses and shrubs, not for trees or in the context of very dynamic environments (Ramakrishnan et al., 2024), see Section 6. The simplest dicothomic stochastic model for vegetation growth and decay reads

$$\dot{\psi} = \begin{cases} -k\psi, & \text{(Decay)} \\ \psi_m - \psi - \mathcal{K}_0|\dot{\eta}|, & \text{(Growth)} \end{cases} \tag{7}$$

where ψ is the vegetation cover, $k = t_g/t_d$ is the ratio between the vegetation growth and decay timescales, while the last term in the growth equation modulates the response of vegetation to sedimentation/erosion ($\mathcal{K}_0$ is an unknown calibration coefficient), and it is active just in type-II vegetation, as commented later.

A crucial aspect of the considered dynamics is to characterize the tolerance thresholds inducing the switching between comfort condition, under which vegetation grows ($\dot{\psi} > 0$), and stressful condition, under which vegetation decays ($\dot{\psi} < 0$). To this end, it is useful to distinguish between two main disturbances: (a) hydraulic flooding induced by wave runup in the swash zone (hereafter referred to as the *runup condition*), which predominantly affects the foreshore region (small X) and (b) wind-induced scouring at the base of vegetation (the *scour condition*), which typically dominates in the backshore and on the dune crest (large X). All terrestrial plant species experience similar stress responses to runup-induced flooding. In contrast, responses to scouring differ markedly, requiring the distinction between two vegetation types (clustering the three types identified by Maun (2009)): (a) Type I vegetation, comprising species with low tolerance to scouring and burial, such as *Helichrysum stoechas*; (b) Type II vegetation, consisting of dune-forming species that are either neutral or benefit from moderate levels of scouring and burial, but only up to a critical threshold, beyond which uprooting or mortality occurs, such as *Ammophila arenaria*.

In the present dimensionless framework, tolerance thresholds are expressed as bounds on the wind parameter F, by imposing that disturbance conditions occur when $F > F_r$ (for runup) and $F > F_s$ (for scour). The evaluation of F_r and F_s is reported below. Overall, at each position X on the dune, the *control threshold* between scour and runup is represented by the lower value between F_s and F_r, that is, the quantity $F_{s|r} = \min(F_s, F_r)$.

3.1. Scour Condition

The scour condition is related to sediment transport of sand grains, a process well represented by the Shields parameter $\tau_* = \tau/\gamma_a D_{50}\Delta$ (where γ_a is the air specific weight, $\Delta \sim 2600$ is the relative density of the sand grain and D_{50} is the mean sediment diameter). After posing $\mathcal{A} = 10^{-3}\epsilon^2/\xi$ and using the definitions $\xi \sim 2.5D_{50}/l$ and $F^2 = u^2/gl$, Equation 6 can be recast to provide the distribution of the Shields parameter τ_* over a dunal topography in a closed form

$$\frac{\tau_*}{AF^2} \equiv \Phi(X) = 1 + f\mathcal{H}(\eta_{,X}). \tag{8}$$

By substituting Equation 4 in the Hilbert transform appearing in Equation 8, one obtains

$$\Phi = 1 + \frac{4\beta f}{\sqrt{\pi}}\{1 - 4(X-1)\mathrm{Da}[2(X-1)]\} + \frac{f\tan\theta_0}{1+X^2}\left(\frac{X}{2} + \frac{\log X}{\pi}\right), \tag{9}$$

where Da[a] refers to the Dawson function (Abramowitz & Stegun, 1964). Examples of spatial profiles of the function $\Phi(X)$ are reported in Figure 2b for typical values of β, evidencing an increase in Φ with β, particularly in proximity of the dune crest.

In the present work, we account for the effect of sediment transport on vegetation in two different ways, according to the type of vegetation that we are considering. For the type-I vegetation, the so called *scour condition* actually corresponds to the disturbance induced by the incipient mobilization of sand grains, namely when the Shields parameter τ_* becomes larger than a critical value. Taking into account the effect of slope on sediment mobilization (Luque & Van Beek, 1976), the scour-condition for type-I vegetation reads

$$\tau_* > \tau_{*c} \cdot g_{s,I}(X), \tag{10}$$

where τ_{*c} is the critical Shields parameter for incipient mobilization for a horizontal surface ($\tau_{*c} \sim 0.02$ for small sand), while $g_{s,I}(X)$ is a correcting function for the critical Shields stress due to the dune local slope $d\eta/dX$ (reported in Appendix A).

The scour condition for the dune-forming species (type-II) is instead related to the deposition/erosion rate $|\dot{\eta}|$. Physically, the threshold between growth and decay is defined as the point at which the rate of deposition or erosion exceeds the vegetation's ability to adapt or keep pace (through the increase in the above-ground or below-ground biomass). In mathematical terms, this corresponds to evaluating the condition such that the growth relationship on the right-hand side of Equation 7 becomes negative and thus meaningless (namely $\mathcal{K}_0|\dot{\eta}| > \psi_m - \psi$). To this end, we need to compute the relationship between $|\dot{\eta}|$ and the wind parameter F. Inspired by Durán Vinent and Moore (2013), we invoke Exner's equation for sediment conservation accompanied by a saltation-relaxation transport model (Sauermann et al., 2001)

$$\frac{d\eta}{dT} = -\mathcal{K}_1\frac{\partial q}{\partial X}, \qquad \frac{\partial q}{\partial X} = \frac{q}{\Lambda}\left(1 - \frac{q}{q_s}\right), \tag{11}$$

where q is the dimensionless sediment transport rate per unit width, q_s its saturation value after relaxation at the saturation length $\Lambda \sim 10^3\xi$ (Hersen et al., 2002) and $\mathcal{K}_1 \sim 31(\xi t_g/l)\sqrt{gD_{50}}$ is a scaling factor due to non-dimensionalization. Furthermore, a classical sediment transport formula that considers vegetation-induced shear stress partition allows q_s to be proportional to the quantity $\tau_*^n/(1+\Gamma\psi)$ where Γ is a dimensionless roughness factor ($\Gamma = 16$, according to Durán Vinent and Moore (2013)). Power law function is typical in sediment transport formulas, for example, in the Engelund-Hansen formulation, $n = 5/2$ (Garcia, 2008).

After resolving q from the second equation of Equation 11 by imposing the boundary condition $q(\Lambda) = q_s$, substituting in the first equation and reminding that ψ is a space-dependent function, we finally get

$$|\dot{\eta}| = \mathcal{K}_1\left|\frac{\Lambda\mathcal{G}(X,\psi)}{I(X)} - 1\right|\frac{F^{2n}}{I(X)}, \qquad q \sim \frac{\mathcal{K}_1\Lambda}{I}F^{2n} \tag{12}$$

where

$$\mathcal{G} = \left(\frac{1+\Gamma\psi}{\Phi(X)}\right)^n, \qquad I = \int_\Lambda^X e^{(\zeta-X)/\Lambda}\mathcal{G}(\zeta,\psi(\zeta))d\zeta. \tag{13}$$

The above solution suggests that sediment transport is proportional to the reciprocal of the integral term I. We also remark that the expression Equation 12 is without approximation and is valid for any dune topography. However, in order to keep the theory on analytical ground, hereafter we will confound the time-dependent term F^{2n} with its average. Furthermore, since Λ is usually $\ll 1$ a Taylor series expansion allows for an approximated analytical form of the integral I (see Supporting Information S1), which leads to a closed solution for Equation 12, namely

$$|\dot{\eta}| \sim \frac{\mathcal{K}_1 \Phi^n |f_1 - n\Lambda f_2|}{\Lambda(1+\Gamma\psi)^n \left[f_1 + n\Lambda f_2 - \Phi\right]^2} \langle F^{2n} \rangle \equiv \mathcal{K}_1 g_{s,II}(X) \cdot \langle F^{2n} \rangle \tag{14}$$

where $f_1 = (\Phi + nX\Phi')e^{1-X/\Lambda}$ and $f_2 = \Phi' - \Gamma\Phi\psi'/(1+\Gamma\psi)$, with the prime referring to space derivation.

Figure 2c illustrates the effect of vegetation on sediment transport, q, assuming, for simplicity, that the spatial distribution of $\psi(X)$ is proportional to the bed topography, with a maximum value ψ_m (more realistic distributions will be derived in Section 4 later on). As expected, increasing vegetation leads to a reduction in sediment transport. Conversely, Figure 2d shows that increasing the crest elevation—while keeping vegetation constant—results in higher sediment transport. This is accompanied by an increase in the magnitude of its spatial gradient, which, according to Equation 11, corresponds to a greater rate of change in bed topography.

We also remark that the maximum shear stress (and hence also the maximum sediment transport) occurs at the dune crest. In contrast, the rate of erosion/deposition, as given by the Exner equation, is related to the spatial gradient of the sediment flux, and is therefore minimal at the crest (Figures 2c and 2d). This explains why the threshold function associated with type II vegetation exhibits a peak at the dune crest (Figure 2f).

With the aid of Equations 4 and 8, the conditions for scouring, for Type I and Type II, can be finally posed in a dimensionless framework, respectively

$$F^2 > \frac{\tau_{*c}}{\mathcal{A}\Phi} g_{s,I} \equiv (F_{s_I})^2. \tag{15}$$

$$F^{2n} > \left(\mathcal{K}_1 g_{s,II}\right)^{-1} (1+\Gamma\psi)^n \left(\psi_m - \psi\right) \equiv (F_{s_{II}})^{2n} \tag{16}$$

Notice that, for type II, there is an interval $F_{s_I} < F < F_{s_{II}}$ wherein sediment transport is active but the vegetation is in the growing state. We also remark the *state-dependency* of the thresholds, that is $F_{s_{II}}$ does depend on the state variable ψ.

3.2. Runup Condition

The runup condition corresponds to the flooding of the site due to wave setup and swash excursion, and it is the dominant mechanism in the swash zone $X \ll 1$. Wave runup depends on the deep water wave height ζ_{dw}, its length l_{dw}, and the beach slope θ_0. For non-dissipative beaches (i.e., when the Iribarren number $I_r = \tan\theta_0 \sqrt{l_{dw}/\zeta_{dw}}$ is >0.3), the 2% exceedance wave runup with respect to the tidal excursion is commonly computed as (Rinaldo et al., 2021; Stockdon et al., 2006)

$$\zeta = g_r(\theta_0)\sqrt{\zeta_{dw} \cdot l_{dw}}, \tag{17}$$

where the function g_r is reported in Appendix A. For the present purposes, we recast even the runup-condition in terms of the wind parameter F, by recalling that the deep water theory suggests $l_{dw} = 2\pi c^2/g$, where the wave celerity c is roughly proportional to u (i.e., $c \sim 0.8u$, cf. Sverdrup and Munk (1952)), while ζ_{dw} has been observed to be roughly consistent with the relation $\zeta_{dw} = ru^2/g$, (Figure 1g provides the distribution of the coefficient r retrieved from ERA5 data set, see also Figure S2 in Supporting Information S1). After simple algebra, the dimensionless form of the runup condition reduces to

$$F^2 > \frac{\eta(X) - a/l}{0.8 \cdot g_r(\theta_0)\sqrt{2\pi r}} \equiv F_r^2, \tag{18}$$

where a is the maximum tidal excursion.

The cusp point in the spatial behavior of $F_{s|r}$ reported in Figure 2f clearly reflects the transition from the *runup-dominated* zone in the swash zone and the *scour-dominated* zone elsewhere.

3.3. Analytical Solutions

The average times that F stays in the decay and growth intervals are, respectively, $\langle T_{F>F_{s|r}} \rangle$ and $\langle T_{F<F_{s|r}} \rangle$. These times depend on the statistical features of the random variable F and are proportional to the (dimensionless) integral scale of the forcing $\mathcal{T} = \mathcal{I}_u / t_g$, via Equation 2. Examples of different pdfs of F with increasing coefficient of variation are reported in Figure 2e, from which it is evident that the overcoming of the threshold is associated with the tails of the distributions. Also, it emerges that, with the increase in the forcing variability, the events under threshold increase, with beneficial effects on vegetation growth.

When approached in a deterministic way, the first equation of the system Equation 7 induces an exponential decay, and the second equation provides a logistic-like growth (Camporeale & Ridolfi, 2006). However, here we address the system Equation 7 by accounting for the stochastic shift induced by the external random forcing $F(T)$. A derivation of the master equation related to the dichotomic problem is reported in Appendix C. The steady-state solution ($T \to \infty$) of the master equation provides the stationary probability density function of the vegetation cover

$$p_\psi = \mathcal{N} \frac{(k-1)\psi + \psi_m - \alpha}{\psi^{1-k_D/k} \left(\alpha + \psi - \psi_m\right)^{1-k_G}}, \tag{19}$$

where

$$\alpha = \mathcal{K} g_{s,II}(X) \cdot \langle F^{2n} \rangle, \quad k_D = \langle T_{F<F_{s|r}} \rangle^{-1}, \qquad k_G = \langle T_{F>F_{s|r}} \rangle^{-1}, \tag{20}$$

while $\mathcal{K} = \mathcal{K}_0 \mathcal{K}_1$ for type II, $\mathcal{K} = 0$ for type I, and $\mathcal{N}$ is a normalization constant to make the pdf have a unitary area, namely $\int_0^{\hat{\psi}} p_\psi d\psi = 1$. It is noteworthy to observe that the solution Equation 19 provides very different shapes depending on the shore-cross coordinate X, with the transition from bell-shaped to exponential distributions in a nonmonotonic way. An example for type I is reported in Figure 2g.

Upon integration, the steady-state solution Equation 19 is adopted to provide analytical expressions for the statistical moments of the probability distribution function p_ψ. For brevity, we report here only the expressions for the mean and variance, noting that the domain of existence of the solution Equation 19 is $\psi = [0, \psi_m - \alpha]$, and that the normalization constant $\mathcal{N}$ must ensure that the probability density function p_ψ integrates to unity over this interval:

$$\mu_\psi = \int_0^{\psi_m - \alpha} p_\psi \psi d\psi = \frac{k_D (\psi_m - \alpha)(k + k_D + k_G)}{(k_D + k_G)(k_G k + k + k_D)}, \tag{21}$$

$$\sigma_\psi^2 = \int_0^{\psi_m - \alpha} p_\psi (\psi - \mu_\psi)^2 d\psi = \frac{k^2 k_D k_G (\alpha - \psi_m)^2 \left[k(k_D + 2k_G + 2) + (k_D + k_G)^2 + 2k_D + k_G\right]}{(k_D + k_G)^2 (k k_G + k + k_D)^2 \left[k(k_G + 2) + k_D\right]}. \tag{22}$$

Equations 19–22 are the main theoretical outcome of the present analysis. To improve the accuracy of the model in the following, the above solutions will be used recursively, iteratively posing $\psi = \langle \psi \rangle$ in the computation of coefficients k_G, k_D, α.

4. Sensitivity Analysis

Reminding that the perturbation parameter ϵ is linked to the relative roughness ξ according to Equation 5, the independent parameters governing the present problem may be grouped into three categories: (a) geometrical features (i.e., relative roughness ξ, slope of the swash zone θ_0, dune steepness β); (b) statistics of the forcing (i.e., mean μ_F, coefficient of variation c_F, and temporal integral scale $\mathcal{T}$, of the wind parameter time series), and (c)

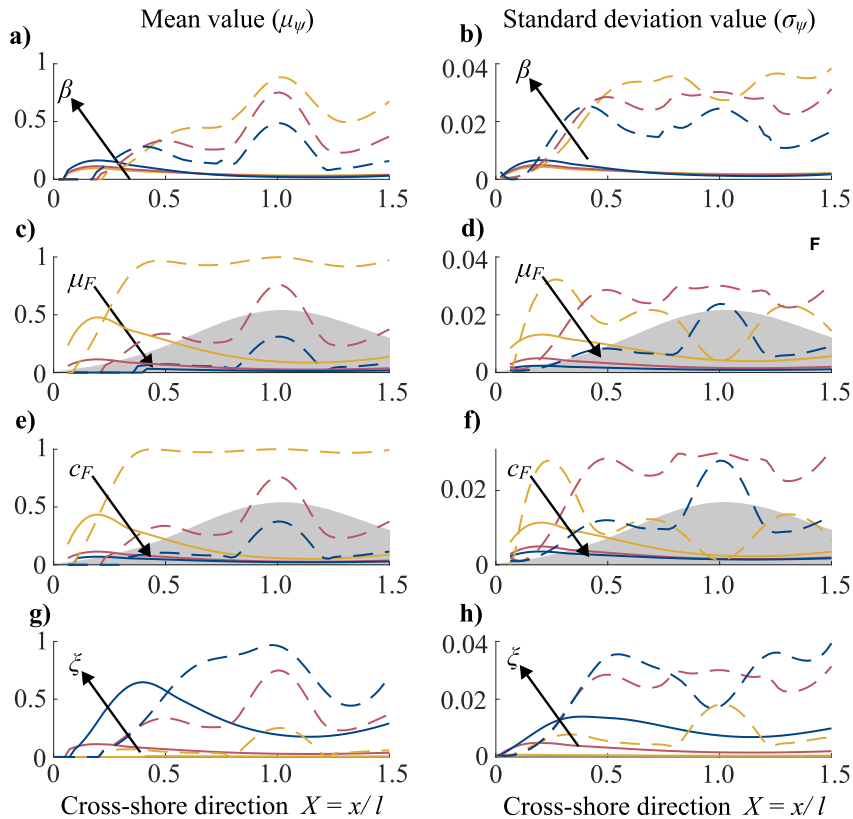

Figure 3. Sensitivity analysis of the mean value μ_ψ (left) and the standard deviation σ_ψ (right) in the cross-shore direction by changing each parameter at once with increasing value from yellow to blue (solid lines: type I; dashed lines: type II). (a, b) $\beta = [0.025, 0.05, 0.1]$; (c, d) $\mu_F = [0.1, 0.15, 0.2]$; (e, f) $c_F = [0.7, 1, 1.2]$; (g, h) $\xi = [2, 20, 100]\cdot 10^{-6}$; $\mathcal{K} = 2$. The gray shading in panels (c–f), report a representative dune topography with $\beta = 0.05$ and $\theta_0 = 6°$. The maximum tidal excursion a has been set to zero for simplicity.

biological features (i.e., $k = t_g/t_d$, $\mathcal{K}$). Nevertheless, the following physical considerations allow further reduction of the parametric space. First, considering a grain size distribution in the range of 0.2–1 mm and a dune wavelength between 25 and 500 m, we obtain $\xi = 2.5D_{50}/l = 10^{-6}$ to 10^{-4}. Second, reasonable values for the growth and decay timescales for grasses and shrubs in dune environments are $t_g = \mathcal{O}(1)$ years and $t_d = \mathcal{O}(1)$ days, respectively, leading to $k = t_g/t_d = \mathcal{O}(300)$. Third, an increase in dune steepness β mirrors an increase in shoreline slope θ_0, due to the associated elevation and threshold increase. Finally, the integral scale $\mathcal{I}_u$ of the wind is typically confined to a narrow range (approximately 1–2 days, as reported in Figure 1g). Consequently, $\mathcal{T} = \mathcal{I}_u/t_g$ marginally affects the sensitivity analysis. In summary, the definitive quadruplet $\{\beta, \mu_F, c_F, \xi(\epsilon)\}$ represents the *controlling parameter space* of the present modeling approach. We remark that these parameters are all well-identifiable through remote sensing or by exploiting ERA5-like data sets, as demonstrated later in the validation, while the coefficient $\mathcal{K}$ is a calibration parameter.

A theoretical exploration of the model's outcomes in the parameter space is described in Figure 3. The results for the spatial distributions of the first and second moments of p_ψ, in the cross-shore direction, show that, due to the threshold patterning, the two types of vegetation perform in quite different ways. Type II (dashed lines) seems to be dominant in the back-shore with a peak in the zone $X = 0.7 - 1.2$, while type I (solid lines) dominates at the front-shore. More specifically, the peak performed by dune building vegetation species (type-II) is related to the high values of the thresholds at the crest, that in the present model are defined as the exceedance of the deposition/erosion rate with respect to the vegetation's ability to adapt or keep pace. This result is in agreement with observations on real coastal dunes (e.g., Demichele et al., 2025), since the dune crest is the place where barely any erosion or deposition takes place, which actually facilitates plant growth, whereas for large enough winds the windward side experiences erosion and thus low vegetation cover; see also Durán Vinent and Herrmann (2006).

Table 1
Geographic Identification and Model Parameters of the Four Pilot Areas (Retrieved From Open Global Data Set)

ID	Location	Coordinates	Area (km^2)	Tide a (m)	Dune height h (m)	Wind μ_F	c_F	$\mathcal{I}_u$ (hours)	d (m)	r	ϵ
CA1	Rancho Guadalupe Dunes Reserve, CA	120.64°W–35.00°N	5.04	1.42	12.5	0.14	1.24	160	341	0.057	0.036
NY1	Fire Island National Seashore, NY	72.93°W–40.71°N	1.36	1.02	4.1	0.01	3.4	28	595	0.46	0.038
OR1	Nehalem Bay State Park, OR	123.94°W–45.69°N	1.1	2.04	15.1	0.038	2.75	39	561	0.059	0.035
OR2	Hornibrook Shore, OR	124.14°W–43.91°N	8.97	1.92	13.8	0.028	2.7	73	553	0.062	0.04

Note. Definitions. a: max tide excursion from FES2014 tide model; h: dune height; μ_F, c_F, $\mathcal{I}_u$: respectively, mean value, coefficient of variation, and dimensionless integral scale of the wind time series, derived from the analysis of ERA5 hourly signals (see Supporting Information S1) corresponding to offshore selected points adjacent to the pilot areas (shapefiles in *Validation_toolbox.zip* in the ZENODO repository at Camporeale and Latella (2025)); d: mean atmospheric boundary layer thickness in the same selected points; r: fitting coefficient of the relation $\zeta_{dw} = ru^2/g$; ϵ: perturbation parameter of Jackson-Hunt theory.

We also remark that in real conditions, when taking into account colonization by plant species over time, dune-building plants outcompete at the back dune areas, where plant cover can easily reach 100%. At the dune crest on the other hand, cover can be lower than 100% because of the presence of secondary stressors like sand transport and salt spray, etc.

An increase in the steepness β induces a decrease for type II and an increase for type I, with important effects on morphodynamics and restoration purposes (see Section 6). Also, variations in magnitude and variability of the forcing (μ_F and c_F) provide significant effects. For example, both parameters increase the extension of the non-vegetated zone l_v (herein identified as points with $\mu_\psi < 0.05$, in particular for type II vegetation, with a maximum value $l_v = 0.45l$ (see Figure 3c). Remarkably, the measure of variability (or uncertainty) in the vegetation distribution at a single point, that is, σ_ψ, is often non-negligible and is particularly sensible to all parameters investigated, including the aspect ratio β. For example, an increase in flow variability c_F is functional to the occurrence of events lower than the mean, with positive effects on vegetation (see again Figure 2). An increase in persistence in the under-threshold states also promotes encroachment. The spatial fluctuations in the statistical variability of the results may also be reflected in the spatial patterning, potentially giving rise to mosaic structures and clustering in reality. Finally, the nearshore zone may evidence a sudden jump in the vegetation for type II (solid curve Figures 2c and 2e), mainly due to the shift from the runup-dominated zone to the scour-dominated zone.

5. Validation

We assessed the performance of the current modeling approach through a formal validation across four pilot areas randomly selected along the U.S. coast. For this purpose, we utilized an open-data based approach by using remote sensing and open access global platforms: (a) multi-spectral satellite imagery, from the Copernicus Sentinel-2 mission (10-m resolution, through Google Earth Engine), and PlanetScope (3-m resolution, through Planet Labs PBC), to compute long-term average of real cover vegetation distributions; (b) high-resolution elevation models (0.5–1 m), retrieved by the National Oceanic and Atmospheric Administration (NOAA)'s Office for Coastal Management via the Digital Coast tool, to obtain the topography of the dune fields; (c) global coastline shapefile from OpenStreetMap (OSM); (d) FES2014 tide model (Lyard et al., 2021); (e) hourly signals of the ERA5 data set, which include offshore wind, boundary layer height, and significant wave height, for the period 2015–2023, to compute the statistical features of the forcing. The biological features of coastal vegetation ($k = t_d/t_g$, $\mathcal{K}$) remained the only unknown parameters, which were set through a calibration of the model (Section 5.2).

5.1. Evaluation of Earth Observation-Derived Vegetation Profiles

Data preparation and image classification were carried out using a suite of algorithms developed by Latella et al. (2021), partially modified to deal with different satellite image collections, and coupled with in-house Python and Matlab scripts for data analysis, enabling the segmentation of multispectral images for the selected areas. This approach allowed us to distinguish between water, sand and vegetation, and accurately map the spatial distribution of vegetation cover across beach-dune transects.

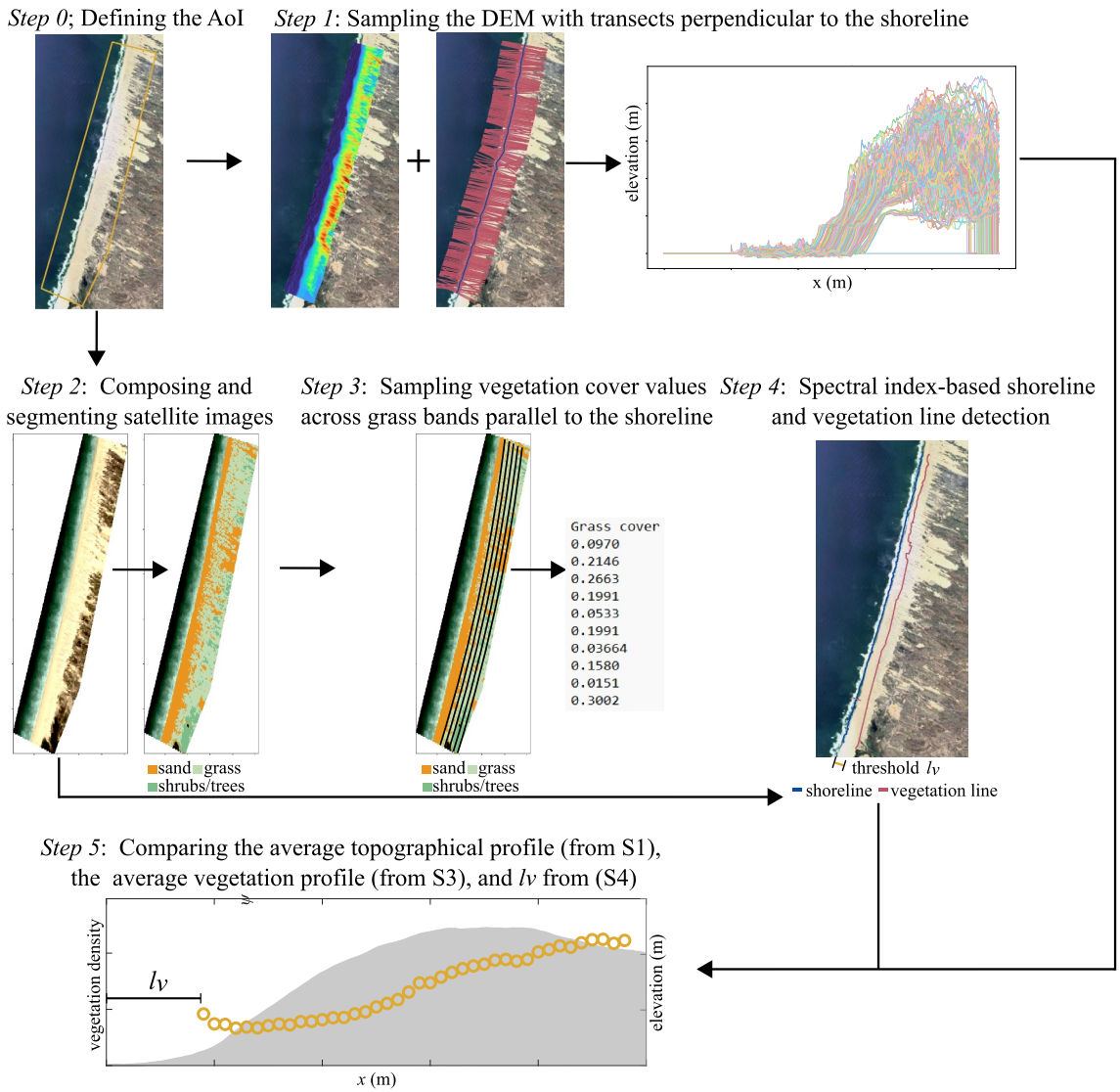

Figure 4. Workflow to obtain representative profiles of the average topographical and vegetation distribution across the beach-dune transects for each pilot area.

We selected four areas of interest (AoIs) along the U.S. coastline (Table 1 and Figure S4 in Supporting Information S1), each represented by rectangles of similar size. The areas were randomly chosen within regions not affected by human activities and covered by the available input data (Table S2 in Supporting Information S1). Each AoI was processed using the workflow described as follows (Figure 4).

After AoI definition (*Step 0*), we generated the AoI average topographical profile by processing digital elevation models (DEMs) and the OSM global shoreline shapefiles (*Step 1*). Relying on the OSM shorelines, we automatically drew equidistant perpendicular transects (spaced 30 m apart) to sample the DEMs, resulting in a series of topographical profiles. We obtained the final profile by averaging this series. Then, we used the core algorithm provided by Latella et al. (2021), which uploads the bounding box shapefile, generates an image collection of satellite images in Google Earth Engine (i.e., the available Sentinel-2 collection and the user-uploaded PlanetScope one), and processes it (*Steps 2–4*). Image collection processing involves filtering based on a specified time range (2017–2024) and cloud cover thresholds, uploading reference data for different land cover classes (water, sand, herbaceous vegetation, trees), and training a random forest model to segment the median composite of the image collection. The algorithm also computes several spectral indices, such as the Normalized Difference Vegetation Index (NDVI) and the Normalized Difference Water Index (NDWI). These indices are used in a thresholding method to discriminate the interface between vegetation and sand (referred to as the *vegetation line*)

Table 2
Calibrated Parameters of the Validation

ID	Location	ψ_m	t_g (days)	$t_{d,I}$ (days)	$t_{d,II}$ (days)	$\mathcal{K}$
CA1	Rancho Guadalupe Dunes Reserve, CA	0.1	60	30	20	0.01
NY1	Fire Island National Seashore, NY	0.2	360	15	1	0.05
OR1	Nehalem Bay State Park, OR	0.7	360	0.3	0.5	0.05
OR2	HornibrookShore, OR	0.3	360	10	0.5	0.05

and to define a more refined shoreline compared to OSM. Additionally, the algorithm generates vegetation cover statistics in the segmented herbaceous-covered area, after temporal averaging over the 2017–2024 period, and longshore spatial averaging along parallel bands (Figure 4).

We remark that the adoption of PlanetScope scenes to substitute or complement Sentinel-2 was already proposed by Doherty et al. (2022). The reference algorithm (Latella et al., 2021) was validated considering the RGB, NIR, and SWIR bands, while we had to modify it to ingest PlanetScope data.

The key outputs of this algorithm are: (a) superposition of the refined shoreline on the DEMs to define the position of $x = 0$ on the topographical profiles, thereby aligning the topography with the algorithm's output; (b) average value of l_v for each AoI, representing the mean distance between the GEE-derived shoreline and the vegetation line; (c) average and standard deviation of the vegetation cover profiles based on the cover percentages within the samples of the herbaceous-covered area.

Finally, the average topographic and vegetation cover profiles were used as benchmarks to compare with the output of the stochastic model (*Step 5*). Details of the classification of each AoI are depicted in Figures S5–S8 in Supporting Information S1.

5.2. Model Setting and Calibration

The setting of the physical parameters of the model was made by using global open data sets (Table S2 in Supporting Information S1). Tidal information was retrieved by the FES2014 tide model (Lyard et al., 2021) applied to the geographic coordinates of a central point in the AoI. We used the model to generate a tide time series for a 19-year recording period, which is the nearest full-year count to the 18.6-year cycle of the lunar node regression, and computed the maximum tide and the mean higher high water (MHHW), which is the average of daily maxima. The characterization of wind and runup forcing (μ_F, c_F, $\mathcal{T}$, d, l and r) followed the same procedure explained for the computation of Figures 1c–1h (details are reported in Supporting Information S1, while the whole ERA5 data products for validation are contained in the open-access ZENODO repository in (Camporeale and Latella (2025)).

The topographic characterization was based on the real topographic mean shape of the dune, rather than using the simplified shape of Equation 4. Therefore, computation of the Hilbert Transform $\mathcal{H}(d\eta/dX)$ of Equation 8 was made through numerical integration. The friction velocity u_* was computed by the analysis of $\mathbf{u}_{10}$ and $\mathbf{u}_{100}$ time series, the wavelength l retrieved from the topographic data, and ξ and ϵ was finally derived by manipulating Equation 5, see also Supporting Information S1.

The only parameters requiring calibration are the biological ones, as the present validation is entirely based on open global data sets. It is important to note that ψ_m is not a critical parameter in the model, as it merely sets the reference value for vegetation cover. Additionally, t_d has no significant effect on the outcomes, since the key factor is the ratio $k = t_g/t_d$. To our knowledge, there is no established value for the parameter $\mathcal{K}$. Finally, we ensured that all calibration parameters were set to physically acceptable values (Table 2).

5.3. Validation Results

The outcome of the validation is reported in Figure 5, wherein the model prediction of the mean vegetation cover $\langle\psi\rangle$ (types I + II, blue solid line) is compared with real values processed by Sentinel-2 (red circles) and PlanetScope (yellow circles) data sets. We note that the overall trends of vegetation cover observed from the S2 and Planet profiles are consistent with each other, though individual values often differ. This can be attributed to

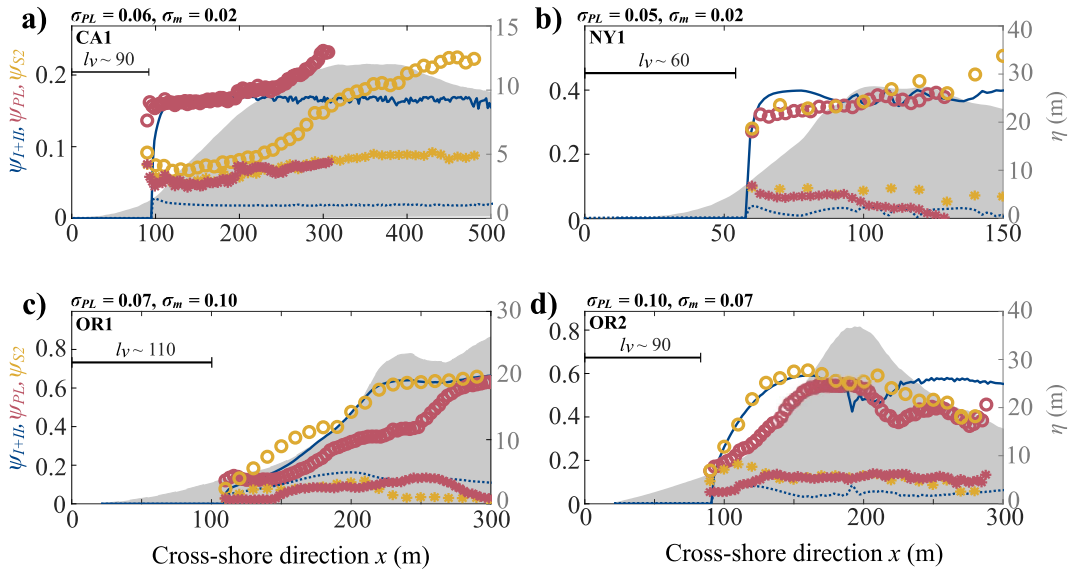

Figure 5. Comparison between average vegetation cover profiles in the cross-shore direction from Earth Observation and the present stochastic model, for four pilot areas in the U.S. Gray shading: long-shore averaged dune topography $\overline{\eta}$ (overline refers to the average over multiple transects within the region of interest); Blue line: model output for the mean (solid) and standard deviation (dashed) for the sum of type I + II; Red and yellow marks: mean (circles) and standard deviation (stars) vegetation cover derived from the analysis of Planet and Sentinel-2 satellite imagery, respectively. The text above the panels reports the long-shore averaged standard deviation of the outcome from Planet imagery, $\overline{\sigma_{PL}}$, and the model's standard deviation, $\overline{\sigma_m}$. Locations: (a) Rancho Guadalupe Dunes Preserve, CA (CA1); (b) Fire Island National Seashore, NY (NY1); (c) Nehalem Bay State Park, OR (OR1); (d) Hornibrook Shore, OR (OR2).

several factors: (a) the varying spatial resolutions of the sensors; (b) the absence of quality flags in PlanetScope data, which made it challenging to fully eliminate noise from saturated or shadowed pixels, although cloud cover likely had minimal impact as PlanetScope images were selected for 0% cloud coverage, while Sentinel-2 images were filtered for a maximum of 30% cloud coverage and further refined through pixel-by-pixel quality checks based on available flags; (c) the lack of shortwave infrared (SWIR) bands, which are frequently used in shoreline and coastal mapping (Vos et al., 2019). Although such a disagreement increases the uncertainty of the benchmark data, taken here as a representation of the real vegetation distribution, it also strongly indicates the future steps to improve our model application and overall EO-based coastal research, which are the need for ground data and a more systematic comparison and cross-validation of products from different sensors, or their data fusion (Collin et al., 2022). For all of the above reasons, intermediate values have been considered to facilitate comparison with the stochastic model.

Interestingly, the model's prediction of l_v is closely aligned with the benchmark across all four pilot areas, while the biological parameters being calibrated within physically acceptable ranges (t_g = 30–360 days, t_d = 0.3–30 days, Table 2). The overall comparison of the distributions is generally highly consistent, in particular when comparing Sentinel-2 and the model's outcomes. However, it is important to note that the relative errors between the model and the benchmark data are always smaller than $\overline{\sigma_{PL}}$ (overline refers to the average over multiple transects), which serves as a proxy for the uncertainty of the satellite product (as explained earlier, $\overline{\sigma_m}$ has a different meaning and is reported here for comparison purposes only).

Moreover, except for OR2, the real cover profiles exhibit monotonically increasing trends, with little tendency to display up-and-down patterns. This can be attributed to two main reasons: (a) Satellite data capture vegetation cover, not biomass density. Although our model assumes a proportional relationship between the two, this is an idealization; in reality, the correlation is not perfect; (b) Image processing does not discriminate among plant species, so the patterns reflect the overall vegetation cover, which typically increases with distance from the shore, and the typical zonation patterns associated with individual species are lost in the aggregated signal. In contrast, the model considers only two types of species, which is particularly evident in the OR1 results.

Finally, the spatial profile of the standard deviation derived from both satellite data sets is also reported (stars), together with the corresponding theoretical value (blue dashed lines). It is important to stress, however, that this comparison can only be interpreted qualitatively, since the two quantities—although similar—carry slightly different meanings. The theoretical standard deviation is obtained from Equation 22 and represents the expected temporal variability of a single realization under the steady-state assumption. In contrast, the standard deviation derived from the satellite data reflects the spatial variability of vegetation cover measured along selected transverse dune profiles. These two quantities can be meaningfully compared only under the assumption of ergodicity, where the spatial and temporal averages are assumed to be equivalent. However, the satellite-based estimate inherently involves greater uncertainty due to two main reasons: (a) Measurement errors associated with the full satellite acquisition and image-processing chain; (b) The transverse profiles used are not topographically identical. Therefore, although they belong to the same general area, they cannot be considered exact physical realizations of the same stochastic process.

6. Discussion and Conclusions

In this study, we developed a threshold-guided, state-dependent dichotomic model to analyze the stochastic dynamics of coastal dune vegetation under the influence of external random disturbances. By incorporating boundary layer theory, wave dynamics, and sediment mechanics, we derived analytical solutions for vegetation cover distribution and its associated uncertainties across dunes, using open global data sets as input. Validation against satellite imagery and high-resolution elevation data from the U.S. coastline confirmed the robustness and accuracy of the model. Our approach complements and extends recent works by Durán Vinent et al. (2021) and Ramakrishnan et al. (2024), by focusing on the effects of random wind disturbances on vegetation distribution within a compound threshold-guided stochastic framework.

The model requires calibration based primarily on biological characteristics of vegetation, such as the ratio between growth and decay timescales and the susceptibility of vegetation to erosion/deposition processes, while the majority of the model parameters can be retrieved through an open-data set approach. Further progress in calibration could be achieved through site-specific field data, a direction for future research (Belcore et al., 2024; Demichele et al., 2025).

More specifically, the classification of plant species and the identification of morphological metrics on real coastal dunes—such as those recently documented in Demichele et al. (2025)—combined with a multi-temporal analysis, could in the future enable the calibration of the model's biological parameters (summarized in Table 2). This would allow the extension of the analysis to a broader range of (non-interacting) species, an objective that will be addressed in future developments.

Furthermore, advancing the theoretical framework will involve incorporating the full coupling between vegetation dynamics and morphodynamics within a stochastic framework, as well as computing recovery times (Vesipa et al., 2016), both of which remain beyond the scope of this study.

The quasi-steady approximation represents a limitation of the theory, arising from the need to derive an analytical solution. This approximation confines the model's applicability to cases where a clear separation exists between the timescales of morphodynamic evolution and vegetation dynamics. In other words, the ratio between these two timescales—which, according to the dimensionless framework, is quantified by $|\dot{\eta}|$—must satisfy the condition $|\dot{\eta}| \ll 1$. By analyzing the range of values predicted by Equation 14, we find that $|\dot{\eta}|$ is typically on the order of $\sim 10^{-1}\langle F^n \rangle$ or less for annual vegetation types (e.g., grasses and shrubs). However, this quantity can increase significantly in the case of perennial vegetation (e.g., trees), with a decreasing trend as the roughness height ξ increases. Once the statistics of $\langle F^n \rangle$ are computed, this condition may be employed to delimit the domain of validity of the model. It appears that the criterion is not universally satisfied. In particular, rapid erosion or accretion events—frequently observed along the ocean-facing slopes of coastal dunes—may violate the quasi-steady assumption. However, it is worth noting that the analytical solution can be recursively iterated, which partially addresses this issue by relaxing the quasi-steady approximation, despite the fact that the exact solution presented is formally a stationary solution of the master equation. In this context, transient solutions, such as those employed in the computation of recovery times, would ultimately resolve the limitation by capturing the full temporal dynamics of the system.

Table 3
Effects of Parameters on the Model Outcomes

Parameter	Frontshore effects	Backshore effects
β	$\uparrow\mu_\psi, \uparrow\sigma_\psi, \downarrow\dot{\eta}$	$\downarrow\mu_\psi, \downarrow\sigma_\psi, \uparrow\dot{\eta}$
μ_F	$\downarrow\mu_\psi$	$\downarrow\mu_\psi$
c_F	$\downarrow\mu_\psi$	$\downarrow\mu_\psi$
ξ	$\uparrow\mu_\psi, \uparrow\sigma_\psi$	$\uparrow\mu_\psi, \uparrow\sigma_\psi$
ψ	$\downarrow\lvert\dot{\eta}\rvert$	$\downarrow\dot{\eta}$

Although the present model does not explicitly simulate the morphological evolution of dunes, the results underscore the critical influence of the initial dune slope on the vegetation establishment and distribution under stochastic forcing. In particular, steeper profiles tend to support denser vegetation cover in the shorefront while limiting colonization near the backshore, suggesting that slope can modulate the spatial organization of plant communities. This insight provides a useful guideline for restoration design: shaping initial dune berms with steeper slopes—within stability constraints—may foster favorable conditions for vegetation development that, in turn, contribute to long-term geomorphic stability. It is also worth reminding a distinction between the initial colonization phase of an unvegetated sand hill (dune), with plants first adaptating to the dominant physical factors including surface changes due to active sand transport, and later stages, where the protective cover of the established dune (where sand transport is negligible due to vegetation cover) allows a complex back dune ecosystem to emerge.

Spatial variability also suggests that planting strategies in restoration efforts may benefit from adaptive density targets: lower planting densities may suffice in the early stages or near the shorefront, while denser, more continuous vegetation cover becomes critical in backshore areas or later successional phases. These findings support the idea that restoration interventions should be spatially and temporally tailored, aligning plant densities with expected disturbance exposure and elevation to enhance the long-term resilience of dune systems. Thus, while the model does not predict topographic change, it offers a conceptual basis to inform the berm geometry in the context of coastal dune restoration.

Different scenarios also depend on the vegetation type. For instance, by synthesizing information from Figures 2 and 3, it can be inferred that regions far backshore ($X > 1.2$) are characterized by type-II vegetation prone to sedimentation, leading to stabilization. In contrast, the frontshore ($X < 1$), under different conditions, can be stabilized by type-I vegetation, particularly at high roughness values that allow for maximum density there (see Figure 3g). As summarized in Table 3, deposition (erosion) rate increases with steepness (β) in the backshore (frontshore), but decreases with vegetation cover ψ, which, in turn, tends to decrease with increasing steepness (Figure 3a). It follows that the development trajectory of a specific shape from an initial state depends on their relative values over time. Initially, a combination of sedimentation (i.e., $\dot{\eta} = -\partial q/\partial X > 0$) and erosion (i.e., $\dot{\eta} = -\partial q/\partial X < 0$) is favored when ψ is low, thus promoting dune building and migration. This process halts if the vegetation has enough time to develop to a level that interferes with sediment transport. Otherwise, a tipping point is surpassed and a stable condition with stationary vegetation patterning never develops. The identification of a morphodynamic tipping point—beyond which vegetation and elevation co-evolve more strongly—can help in timing interventions, such as supplemental planting or reshaping so to ensure that positive feedbacks are initiated, rather than relying on natural progression alone.

Coastal dune restoration encompasses a range of interventions, from re-vegetation and stabilization to promoting dune mobility through de-vegetation (Lithgow et al., 2013). Designing effective restoration strategies requires a comprehensive understanding of coastal eco-morphodynamics. Our model and the analytical tools it provides, such as the computation of free-vegetation width l_v, offer practical support for nature-based coastal restoration projects. These tools can aid decision makers in predicting the behavior of coastal ecotones under different scenarios, thus guiding policymakers toward informed site-specific restoration plans. In doing so, we can produce reliable tools for managing dune systems and assessing their response to external forces and human activities.

Appendix A: Correction Functions $g_{s,I}$ and g_r

The correction function $g_{s,I}$ has been derived from the classical force equilibrium for a single particle on a slope, balancing gravitational force and Coulomb resistance (Luque & Van Beek, 1976). The correction function g_r has been empirically derived for wave runup by Stockdon et al. (2006). The two functions read, respectively

$$g_{s,I} = \cos\theta\left(1 + \frac{\theta}{\nu_c}\right), \quad g_r = \tan\theta_0\left[0.38 + \left(0.172 + \frac{0.001}{\tan^2\theta_0}\right)^{1/2}\right], \tag{A1}$$

where $\theta = \arctan(-d\eta/dX)$ is the local slope of the dune, θ_0 its value on the shoreline, and $\nu_c \sim 0.6$ is the Coulomb coefficient for sands.

Appendix B: Relationships for the Coefficients k_D,k_G

$$k_D = \frac{e^{-\hat{F}}}{\mathcal{T}E(1-q,\hat{F})}, \quad k_G = \frac{e^{-\hat{F}}\hat{F}^q}{\mathcal{T}(1-\Gamma_{q,\hat{F}})\Gamma_q} \tag{B1}$$

where $q = c_u^{-2}$, $\hat{F} = qF_{s|r}/\mu_F$, $E(a,z)$ is the exponential integral function, $\Gamma_q = \int_0^\infty t^{q-1}e^{-t}dt$ is a shorthand for the Euler Gamma function and $\Gamma_{a,b} = \int_b^\infty t^{a-1}e^{-t}dt$ is a shorthand for the incomplete Gamma function (Abramowitz & Stegun, 1964).

Appendix C: Master Equation

By appealing to the theory of stochastic differential equations (Ridolfi et al., 2011), the two model Equation 7 can be combined into a single stochastic ordinary differential equation forced by a dichotomic Markov noise

$$\frac{d\psi}{dt} = f(\psi) + g(\psi)\zeta(t), \tag{C1}$$

where $\zeta(t)$ is a dichotomic Markov noise, which can assume only two values (Δ_D and Δ_G). Accordingly, the function $f(\psi)$ and $g(\psi)$ are chosen such that when $\zeta = \Delta_D$, Equation C1 reduces to the first line of Equation 7, while when $\zeta(t) = \Delta_G$, it reduces to the second line. We can also assume that the dichotomic noise, $\zeta(t)$, has a vanishing average value, namely $T_D\Delta_D + T_G\Delta_G = 0$, where T_D and T_G are the mean duration of decay and growth periods, respectively equal to the reciprocal of the shifting rates between the two states:

$$k_D = T_G^{-1} = \langle T_{F<F_{s|r}}\rangle^{-1}, \qquad k_G = T_D^{-1} = \langle T_{F>F_{s|r}}\rangle^{-1}. \tag{C2}$$

Since, without any loss of generality we may set $\Delta_D = 1$, we finally get:

$$f(\psi) = -\frac{k_G k\psi + k_D(\alpha+\psi-\psi_m)}{k_D+k_G}, \qquad g(\psi) = \frac{k_D(\alpha+\psi-k\psi-\psi_m)}{k_D+k_G}, \tag{C3}$$

where $\alpha = \mathcal{K}g_{s,II}(X)\cdot\langle F^{2n}\rangle$, and $\mathcal{K} = \mathcal{K}_0\mathcal{K}_1$ for type II, while $\mathcal{K} = 0$ for type I. The corresponding master equation for Equation C1 reads (Horsthemke & Lefever, 1984)

$$\frac{\partial p_\psi}{\partial t} = -\mathcal{Z}_0 p_\psi + \frac{\mathcal{Z}_1^2}{k_D k_G}\frac{\partial p_\psi}{\partial \psi}\int_{-\infty}^{t}\mathcal{Z}_1\frac{\partial(gp_\psi)}{\partial\psi}e^{-[\mathcal{Z}_0+k_D+k_G](t-t')}dt', \tag{C4}$$

where:

$$\mathcal{Z}_0 = \frac{\partial}{\partial\psi}\left[f + \frac{k_G\Delta_G - k_D\Delta_D}{k_G+k_D}g\right], \qquad \mathcal{Z}_1 = \frac{(\Delta_G-\Delta_D)k_G k_D}{k_G+k_D}. \tag{C5}$$

The stationary solution of Equation C4 reads (Kitahara et al., 1980)

$$p_\psi = g\mathcal{Z}e^{-\int f(\psi')k_D\mathcal{Z}d\psi'}, \quad \text{with} \quad \mathcal{Z}(\psi) = -\frac{(k_D+k_G)f}{k\psi(\psi_m-\alpha-\psi)}. \tag{C6}$$

After substituting Equation C3 in Equation C6 one obtains Equation 19.

Notation

β	Dune steepness, defined as $\beta = h/l$ [−]
c_F	Coefficient of variation of the wind parameter time series [−]
c_u	Coefficient of variation of wind speed [−]
D_{50}	Median sediment diameter [L]
d	Atmospheric boundary layer height [L]
Δ	Relative density of sand (typically 2600) [−]
ϵ	Ratio of friction to mean wind velocity, u_*/u [−]
$E(a,z)$	Exponential integral function [−]
F	Windy Froude-like number, $F = u/\sqrt{gl}$ [−]
F_r	Runup disturbance threshold [−]
F_s	Scour disturbance threshold [−]
$F_{s\|r}$	Minimum of runup and scour thresholds, $\min(F_s, F_r)$ [−]
γ_a	Specific weight of air [N M^{-3}]
g	Gravity acceleration [L T^{-2}]
h	Dune height [L]
h_m	Height of the middle layer of the boundary layer [L]
k	Ratio of vegetation growth to decay timescales, t_g/t_d [−]
κ	von Kármán constant (~ 0.41) [−]
l	Half-width of the dune [L]
$\mathcal{A}$	Scaling coefficient for the Shields parameter [−]
$\mathcal{I}_u$	Integral timescale of wind [T]
$\mathcal{K}$	Sediment-vegetation coupling coefficient [−]
μ_u	Mean wind speed [L T^{-1}]
$\Phi(X)$	Spatially variable multiplier in τ_* expression [−]
$\psi(x,t)$	Dimensionless vegetation cover index [−]
ψ_m	Maximum vegetation cover index [−]
q	Shape parameter of the Gamma distribution [−]
τ	Shear stress on the bed [Pa]
τ_*	Shields parameter [−]
T	Dimensionless time, $T = t/t_g$ [−]
$\mathcal{T}$	Dimensionless integral timescale of wind $\mathcal{T} = \mathcal{I}_u/t_g$ [−]
t_d, t_g	Vegetation decay and growth timescale [T]
$u(t)$	Wind speed at the middle layer of the boundary layer [L/T]
$\mathbf{u}_{10}$, $\mathbf{u}_{100}$	Wind velocity at 10 and 100 m height [L/T]
x	Cross-shore spatial coordinate [L]

ξ	Relative roughness, $\xi = z_0/l$ [−]
$\zeta(t)$	Daily maximum runup [L]
ζ_{dw}	Significant height of wind waves [L]
z_0	Roughness length [L]
$\eta(x)$	Dimensionless dune topography [−]
θ_0	Swash zone slope angle [rad]

Conflict of Interest

The authors declare no conflicts of interest relevant to this study.

Data Availability Statement

The whole data set generated in this study and the Matlab codes to generate Figures 1 and 5 are deposited in the ZENODO repository https://doi.org/10.5281/zenodo.15516692 (Camporeale & Latella, 2025). Specifically: (a) The zipped file "wind_analysis.zip" containing data sets and scripts used for the characterization of the wind and runup disturbance reported in Figures 1c–1h and contains: (a) The matlab scripts Fig1_generator.m (the main script), extract_new.m; (b) 11 folders containing the shapefiles of the offshore zones and the NetCDF files of the ERA5 hourly signals for the period 2019–2022. (b) The zipped file validation_toolbox.zip containing data sets and scripts used for the validation: (a) The matlab scripts Fig5_generator.m (the main script), model_realcase.m, extract.m; (b) Four folders containing all the data set of the pilot areas, including shapefiles of the terrestrial areas, shapefiles of the offshore zone, NetCDF files of the ERA5 hourly signals, mean transect profile, Planet cover profile, Sentinel2 cover profile, high-resolution DEMs.

Acknowledgments

The authors wish to thank Orencio Duran Vinent for his valuable suggestions regarding the modeling aspects. This study was carried out within the "Eco-geomorphic carbon pumping from rivers to blue carbon Ecosystems (e-Capture)" project—funded by the European Union—Next Generation EU within the PRIN 2022 program (D.D. 104—02/02/2022 Ministero dell'Università e della Ricerca) CUP E53D23004070006 and by the European Union (project Grant Agreement no. 101185000—CONCERTO—HORIZON-CL5-2024-D1-01). Views and opinions expressed are however those of the authors only and do not necessarily reflect those of the European Union or the European Climate, Infrastructure and Environment Executive Agency (CINEA). Neither the European Union nor the granting authority can be held responsible for them. Open access publishing facilitated by Politecnico di Torino, as part of the Wiley - CRUI-CARE agreement.

References

Abramowitz, M., & Stegun, I. A. (1964). *Handbook of mathematical functions with formulas, graphs, and mathematical tables*. Dover. New York City.

Baas, A. C., & Nield, J. (2007). Modelling vegetated dune landscapes. *Geophysical Research Letters*, *34*(6). https://doi.org/10.1029/2006gl029152

Bakker, J., Berg, M., Grootjans, A., Olff, H., Schrama, M., Reijers, V., & Van der Heide, T. (2023). Biogeomorphological aspects of a model barrier island and its surroundings—Interactions between abiotic conditions and biota shaping the tidal and terrestrial landscape: A synthesis. *Ocean & Coastal Management*, *239*, 106624. https://doi.org/10.1016/j.ocecoaman.2023.106624

Barbour, M. G. (1978). Salt spray as a microenvironmental factor in the distribution of beach plants at Point Reyes, California. *Oecologia*, *32*(2), 213–224. https://doi.org/10.1007/bf00366073

Barbour, M. G., De Jong, T. M., & Pavlik, B. M. (1985). Marine beach and dune plant communities. In *Physiological ecology of North American plant communities* (pp. 296–322). Springer.

Beaumont, N. J., Jones, L., Garbutt, A., Hansom, J., & Toberman, M. (2014). The value of carbon sequestration and storage in coastal habitats. *Estuarine, Coastal and Shelf Science*, *137*, 32–40. https://doi.org/10.1016/j.ecss.2013.11.022

Bel, G., & Ashkenazy, Y. (2014). The effects of psammophilous plants on sand dune dynamics. *Journal of Geophysical Research: Earth Surface*, *119*(7), 1636–1650. https://doi.org/10.1002/2014jf003170

Belcore, E., Latella, M., Piras, M., & Camporeale, C. (2024). Enhancing precision in coastal dunes vegetation mapping: Ultra-high resolution hierarchical classification at the individual plant level. *International Journal of Remote Sensing*, *45*(13), 4527–4552. https://doi.org/10.1080/01431161.2024.2354135

Bertagni, M., Perona, P., & Camporeale, C. (2018). Parametric transitions between bare and vegetated states in water-driven patterns. *Proceedings of the National Academy of Sciences*, *115*(32), 8125–8130. https://doi.org/10.1073/pnas.1721765115

Bird, E. C. (2011). *Coastal geomorphology: An introduction*. John Wiley & Sons.

Camporeale, C., & Latella, M. (2025). Dataset and codes inherent to the JGR: Earth Surface submission "Stochastic dynamics of coastal dune vegetation" [Dataset]. *(Zenodo repository)*. https://doi.org/10.5281/zenodo.15516692

Camporeale, C., & Ridolfi, L. (2006). Riparian vegetation distribution induced by river flow variability: A stochastic approach. *Water Resources Research*, *42*(10). https://doi.org/10.1029/2006wr004933

Charbonneau, B. R., Duarte, A., Swannack, T. M., Johnson, B. D., & Piercy, C. D. (2022). DOONIES: A process-based ecogeomorphological functional community model for coastal dune vegetation and landscape dynamics. *Geomorphology*, *398*, 108037. https://doi.org/10.1016/j.geomorph.2021.108037

Collin, A., Feunteun, É., & James, D. (2022). Towards better coastal mapping using fusion of high temporal SENTINEL-2 and PLANETSCOPE-2 Imageries: 12 Bands at 3 M through neural network modelling. *ISPRS International Archives of the Photogrammetry, Remote Sensing and Spatial Information Sciences*(43), 479–484. https://doi.org/10.5194/isprs-archives-xliii-b3-2022-479-2022

Davidson-Arnott, R. (2010). *An introduction to coastal processes and geomorphology*. Cambridge University Press.

de Castro, F. (1995). Computer simulation of the dynamics of a dune system. *Ecological Modelling*, *78*(3), 205–217. https://doi.org/10.1016/0304-3800(93)e0090-p

de Luna, M., Parteli, E., Durán, O., & Herrmann, H. (2011). Model for the genesis of coastal dune fields with vegetation. *Geomorphology*, *129*(3–4), 215–224. https://doi.org/10.1016/j.geomorph.2011.01.024

Demichele, D., Belcore, E., Piras, M., & Camporeale, C. (2025). Species-by-species pattern analysis of coastal dune vegetation. *Journal of Geophysical Research: Biogeosciences*, *130*(2), e2024JG008419. https://doi.org/10.1029/2024JG008419

Disraeli, D. (1984). The effect of sand deposits on the growth and morphology of Ammophila breviligulata. *Journal of Ecology*, *72*(1), 145–154. https://doi.org/10.2307/2260010

Doherty, Y., Harley, M. D., Vos, K., & Splinter, K. D. (2022). A Python toolkit to monitor sandy shoreline change using high-resolution planetscope cubesats. *Environmental Modelling & Software*, *157*, 105512. https://doi.org/10.1016/j.envsoft.2022.105512

Doody, J. P. (2013). Coastal squeeze and managed realignment in southeast England, does it tell us anything about the future? *Ocean & Coastal Management*, *79*, 34–41. https://doi.org/10.1016/j.ocecoaman.2012.05.008

Du, J., & Hesp, P. A. (2020). Salt spray distribution and its impact on vegetation zonation on coastal dunes: A review. *Estuaries and Coasts*, *43*(8), 1885–1907. https://doi.org/10.1007/s12237-020-00820-2

Durán Vinent, O., & Herrmann, H. J. (2006). Vegetation against dune mobility. *Physical Review Letters*, *97*(18), 188001. https://doi.org/10.1103/physrevlett.97.188001

Durán Vinent, O., & Moore, L. J. (2013). Vegetation controls on the maximum size of coastal dunes. *Proceedings of the National Academy of Sciences*, *110*(43), 17217–17222. https://doi.org/10.1073/pnas.1307580110

Durán Vinent, O., & Moore, L. J. (2015). Barrier island bistability induced by biphysical interactions. *Nature Climate Change*, *5*, 158–162.

Durán Vinent, O., Moore, L. J., Goldstein, E. B., De Vries, S., Durán Vinent, O., & Ruggiero, P. (2019). Exploring marine and aeolian controls on coastal foredune growth using a coupled numerical model. *Journal of Marine Science and Engineering*, *7*(13), 13. https://doi.org/10.3390/jmse7010013

Durán Vinent, O., Schaffer, B., & Rodriguez-Iturbe, I. (2021). Stochastic dynamics of barrier island elevation. *Proceedings of the National Academy of Sciences*, *118*(1), e2013349118. https://doi.org/10.1073/pnas.2013349118

Durán Vinent, O., Silva, M. V. N., Bezerra, L. J. C., Herrmann, H. J., & Maia, L. P. (2008). Measurements and numerical simulations of the degree of activity and vegetation cover on parabolic dunes in north-eastern Brazil. *Geomorphology*, *102*(3–4), 460–471. https://doi.org/10.1016/j.geomorph.2008.05.011

Fowler, A. (2011). *Mathematical geoscience*. Springer.

Garcia, M. (2008). *Sedimentation engineering: Processes, measurements, modeling, and practice*. Amer Society of Civil Engineers.

Goldstein, E. B., Moore, L. J., & Durán Vinent, O. (2017). Lateral vegetation growth rates exert control on coastal foredune hummockiness and coalescing time. *Earth Surface Dynamics*, *5*(3), 417–427.

Hallegate, S., Green, C., Nicholls, R. J., & Corfee-Morlot, J. (2013). Future flood losses in major coastal cities. *Nature Climate Change*, *3*(9), 802–806. https://doi.org/10.1038/nclimate1979

Hersen, P., Douady, S., & Andreotti, B. (2002). Relevant length scale of barchan dunes. *Physical Review Letters*, *89*(26), 264301. https://doi.org/10.1103/physrevlett.89.264301

Hesp, P. A. (1991). Ecological processes and plant adaptations on coastal dunes. *Journal of Arid Environments*, *21*(2), 165–191. https://doi.org/10.1016/s0140-1963(18)30681-5

Horsthemke, E., & Lefever, R. (1984). *Noise-induced transitions: Theory and applications in physics, chemistry and biology*. Springer. Berlin.

Hunt, J. C. R., Leibovich, S., & Richards, K. J. (1988). Turbulent shear flows over low hills. *Quarterly Journal of the Royal Meteorological Society*, *114*(484), 1435–1470. https://doi.org/10.1002/qj.49711448405

Kang, B., Feagin, R., Huff, T., & Duran Vinent, O. (2024). Stochastic properties of coastal flooding events—Part 2: Probabilistic analysis. *Earth Surface Dynamics*, *12*(1), 105–115. https://doi.org/10.5194/esurf-12-105-2024

Keijsers, J. G. S., De Groot, A. V., & Riksen, M. J. P. M. (2016). Modeling the biogeomorphic evolution of coastal dunes in response to climate change. *Journal of Geophysical Research: Earth Surface*, *121*(6), 1161–1181. https://doi.org/10.1002/2015jf003815

Kitahara, K., Horsthemke, W., Lefever, R., & Inaba, Y. (1980). Phase diagrams of noise induced transitions: Exact results for a class of external coloured noise. *Progress of Theoretical Physics*, *64*(4), 1233–1247. https://doi.org/10.1143/PTP.64.1233

Kroy, K., Sauermann, G., & Herrmann, H. J. (2002). Minimal model for sand dunes. *Physical Review Letters*, *88*(5), 054301. https://doi.org/10.1103/physrevlett.88.054301

Laing, C. C. (1958). Studies in the ecology of Ammophila breviligulata. I. Seedling survival and its relation to population increase and dispersal. *Botanical Gazette*, *119*(4), 208–216. https://doi.org/10.1086/335981

Laio, F., Porporato, A., Ridolfi, L., & Rodriguez-Iturbe, I. (2001). Mean first passage times of processes driven by white shot noise. *Physical Review E - Statistical Physics, Plasmas, Fluids, and Related Interdisciplinary Topics*, *63*(3), 036105. https://doi.org/10.1103/PhysRevE.63.036105

Latella, M., Luijendijk, A., Moreno-Rodenas, A. M., & Camporeale, C. (2021). Satellite image processing for the coarse-scale investigation of sandy coastal areas. *Remote Sensing*, *13*(22), 4613. https://doi.org/10.3390/rs13224613

Lithgow, D., Martínez, M., Gallego-Fernández, J., Hesp, P., Flores, P., Gachuz, S., et al. (2013). Linking restoration ecology with coastal dune restoration. *Geomorphology*, *199*, 214–224. https://doi.org/10.1016/j.geomorph.2013.05.007

Luque, F. R., & Van Beek, R. (1976). Erosion and transport of bed sediment. *Journal of Hydraulic Research*, *14*, 127–144.

Lyard, F. H., Allain, D. J., Cancet, M., Carrère, L., & Picot, N. (2021). FES2014 global ocean tide atlas: Design and performance. *Ocean Science*, *17*(3), 615–649. https://doi.org/10.5194/os-17-615-2021

Macreadie, P., Anton, A., Raven, J., Beaumont, N., Connolly, R., Friess, D., et al. (2019). The future of blue carbon science. *Nature Communications*, *10*(1), 3998. https://doi.org/10.1038/s41467-019-11693-w

Martínez, M., Psuty, N., & Lubke, R. (2008). A perspective on coastal dunes. In *Coastal dunes* (pp. 3–10). Springer.

Maun, M. A. (2009). *The biology of coastal sand dunes*. Oxford University Press.

Moore, L. J., Durán Vinent, O., & Ruggiero, P. (2016). Vegetation control allows autocyclic formation of multiple dunes on prograding coasts. *Geology*, *44*(7), 559–562. https://doi.org/10.1130/g37778.1

Nishimori, H., & Tanaka, H. (2001). A simple model for the formation of vegetated dunes. *Earth Surface Processes and Landforms*, *26*(10), 1143–1150. https://doi.org/10.1002/esp.258

Nolet, C., van Puijenbroek, M., Suomalainen, J., Limpens, J., & Riksen, M. (2018). UAV-imaging to model growth response of marram grass to sand burial: Implications for coastal dune development. *Aeolian Research*, *31*, 50–61. https://doi.org/10.1016/j.aeolia.2017.08.006

Oosting, H. J. (1945). Tolerance to salt spray of plants of coastal dunes. *Ecology*, *26*(1), 85–89. https://doi.org/10.2307/1931917

Ramakrishnan, K., Rinaldo, T., Rodriguez-Iturbe, I., & Durán Vinent, O. (2024). Permanent loss of barrier island resilience due to a critical transition in dune ecosystems. *Communications Earth & Environment*, *5*(447), 437–480. https://doi.org/10.1038/s43247-024-01611-4

Reimann, L., Vafeidis, A. T., & Honsel, L. E. (2023). Population development as a driver of coastal risk: Current trends and future pathways. *Cambridge Prisms: Coastal Futures*, *1*, e14. https://doi.org/10.1017/cft.2023.3

Ridolfi, L., D'Odorico, P., & Laio, F. (2011). *Noise-induced phenomena in the environmental sciences*. Cambridge University Press.

Rinaldo, T., Ramakrishnan, K., Rodriguez-Iturbe, I., & Durán Vinent, O. (2021). Probabilistic structure of events controlling the after-storm recovery of coastal dunes. *Proceedings of the National Academy of Sciences*, *118*(1), e2013254118. https://doi.org/10.1073/pnas.2013254118

Roelvink, D., & Costas, S. (2019). Coupling nearshore and aeolian processes: XBeach and Duna process-based models. *Environmental Modelling & Software*, *115*, 98–112. https://doi.org/10.1016/j.envsoft.2019.02.010

Sauermann, G., Kroy, K., & Herrmann, H. J. (2001). Continuum saltation model for sand dunes. *Physical Review E - Statistical Physics, Plasmas, Fluids, and Related Interdisciplinary Topics*, *64*(3), 031305. https://doi.org/10.1103/PhysRevE.64.031305

Stockdon, H. F., Holman, R. A., Howd, P. A., & Sallenger, A. H., Jr. (2006). Empirical parametrization of setup, swash and runup. *Coastal Engineering*, *53*(7), 573–588. https://doi.org/10.1016/j.coastaleng.2005.12.005

Sverdrup, H. U., & Munk, W. H. (1952). *Wind, sea and swell: The theory of relations for forecasting (No. 303)*. US Government Printing Office.

Toimil, A., Losada, I. J., Nicholls, R. J., Dalrymple, R. A., & Stive, M. J. (2020). Addressing the challenges of climate change risks and adaptation in coastal areas: A review. *Coastal Engineering*, *156*, 103611. https://doi.org/10.1016/j.coastaleng.2019.103611

Van Dijk, P., Arens, S., & Van Boxel, J. (1999). Aeolian processes across transverse dunes. II: Modelling the sediment transport and profile development. *Earth Surface Processes and Landforms*, *24*(4), 319–333. https://doi.org/10.1002/(sici)1096-9837(199904)24:4<319::aid-esp963>3.0.co;2-m

Vesipa, R., Camporeale, C., & Ridolfi, L. (2016). Recovery times of riparian vegetation. *Water Resources Research*, *52*(4), 2934–2950. https://doi.org/10.1002/2015WR018490

Vos, K., Splinter, K. D., Harley, M. D., Simmons, J. A., & Turner, I. L. (2019). CoastSat: A Google Earth Engine-enabled Python toolkit to extract shorelines from publicly available satellite imagery. *Environmental Modelling & Software*, *122*, 104528. https://doi.org/10.1016/j.envsoft.2019.104528

Wilson, J. B., & Sykes, M. T. (1999). Is zonation on coastal sand dunes determined primarily by sand burial or by salt spray? A test in New Zealand dunes. *Ecology Letters*, *2*(4), 233–236. https://doi.org/10.1046/j.1461-0248.1999.00084.x

Yizhaq, H., Ashkenazy, Y., Levin, N., & Tsoar, H. (2013). Spatiotemporal model for the progression of transgressive dunes. *Physica A*, *392*(19), 4502–4515. https://doi.org/10.1016/j.physa.2013.03.066

Zarnetske, P. L., Hacker, S. D., Seabloom, E. W., Ruggiero, P., Killian, J. R., Maddux, T. B., & Cox, D. (2012). Biophysical feedback mediates effects of invasive grasses on coastal dune shape. *Ecology*, *93*(6), 1439–1450. https://doi.org/10.1890/11-1112.1